

PAPER • OPEN ACCESS

## Scrape-off layer (SOL) power width scaling and correlation between SOL and pedestal gradients across L, I and H-mode plasmas at ASDEX Upgrade

To cite this article: D Silvagni *et al* 2020 *Plasma Phys. Control. Fusion* **62** 045015

View the [article online](#) for updates and enhancements.

### Recent citations

- [Turbulence driven widening of the near-SOL power width in ASDEX Upgrade H-Mode discharges](#)  
T. Eich *et al*






**IOP | ebooks™**

Bringing together innovative digital publishing with leading authors from the global scientific community.

Start exploring the collection—download the first chapter of every title for free.

# Scrape-off layer (SOL) power width scaling and correlation between SOL and pedestal gradients across L, I and H-mode plasmas at ASDEX Upgrade

D Silvagni<sup>1,2</sup> , T Eich<sup>1</sup> , M Faitsch<sup>1</sup> , T Happel<sup>1</sup> , B Sieglin<sup>1</sup>, P David<sup>1</sup>, D Nille<sup>1</sup> , L Gil<sup>3</sup> , U Stroth<sup>1,2</sup>, the ASDEX Upgrade team<sup>4</sup> and the EUROfusion MST1 team<sup>5</sup>

<sup>1</sup>Max-Planck-Institut für Plasmaphysik, Boltzmannstr. 2, D-85748 Garching, Germany

<sup>2</sup>Physik-Department E28, Technische Universität München, James-Franck-Str. 1, D-85748 Garching, Germany

<sup>3</sup>Instituto de Plasmas e Fusão Nuclear, Instituto Superior Técnico, Universidade Lisboa, PT, Portugal

E-mail: [davide.silvagni@ipp.mpg.de](mailto:davide.silvagni@ipp.mpg.de)

Received 11 November 2019, revised 16 January 2020

Accepted for publication 11 February 2020

Published 26 February 2020



CrossMark

## Abstract

A cross-regime (L-mode, I-mode and H-mode) database combining scrape-off layer (SOL) power decay length  $\lambda_q$  divertor measurements and upstream SOL electron pressure, temperature and density decay lengths has been assembled at ASDEX Upgrade. It is found that a cross-regime  $\lambda_q$  scaling is best described by a local edge quantity, such as the edge electron pressure evaluated at  $\rho_{\text{poi}} = 0.95$ . Furthermore,  $\lambda_q$  exhibits a clear correlation with edge electron pressure gradient lengths, no matter if taken inside or outside the separatrix. In addition, the database reveals that SOL and pedestal electron pressure gradients are remarkably well correlated across all confinement regimes. The physical interpretation of this observation is discussed with regard to an edge pressure critical gradient paradigm governing the edge physics and to a turbulence spreading in the SOL. Moreover, it is shown that the Spitzer–Härm electron conduction regime is a reasonable approximation to estimate  $\lambda_q$  across different confinement regimes. The main implication of these findings is that a widening of  $\lambda_q$  is linked to a reduction of edge electron pressure gradients.

Keywords: power exhaust, scrape-off-layer, divertor, tokamak, L-mode, I-mode, H-mode

(Some figures may appear in colour only in the online journal)

## 1. Introduction

Power exhaust is one of the key challenges on the way to commercial fusion power plants. In a diverted tokamak, the power crossing the separatrix enters a region called the scrape-off layer (SOL), which is characterized by magnetic field lines intercepting the first wall. The related heat flux, if not lost by volumetric processes in the SOL, reaches the divertor target plates and must not exceed material limits [1]. One of the key quantities that sets the peak heat flux entering the divertor chamber is the so-called exponential power decay

<sup>4</sup> See Meyer *et al* 2019 (<https://doi.org/10.1088/1741-4326/ab18b8>) for the ASDEX Upgrade team.

<sup>5</sup> See Labit *et al* 2019 (<https://doi.org/10.1088/1741-4326/ab2211>) for the EUROfusion MST1 team.



Original content from this work may be used under the terms of the [Creative Commons Attribution 3.0 licence](https://creativecommons.org/licenses/by/3.0/). Any further distribution of this work must maintain attribution to the author(s) and the title of the work, journal citation and DOI.

length in the SOL,  $\lambda_q$ . The value of this quantity strongly affects the operational window of ITER and of any other next step fusion device in terms of the permissible values of the fusion power and power gain  $Q$  [2–4].

Even though in the last years some progress has been made in the fundamental understanding of what sets the power fall-off length [5–7], it remains mainly an empirical science governed by scaling laws. In this respect, a major effort was carried out in 2011 in assembling a multi-machine database of H-mode power decay lengths [8], which have been evaluated between Edge Localized Modes (ELMs) [9, 10]. It was shown that  $\lambda_q$  scales approximately inversely with the poloidal magnetic field at the outer midplane and that such scaling is independent of machine size. More recently, a new attempt to find a cross-regime (L, I and H-mode)  $\lambda_q$  scaling was carried out at Alcator C-Mod [11]. It was found that the power decay length exhibits a dependence on volume-averaged core plasma pressure across all confinement regimes analyzed,  $\lambda_q \propto \bar{p}^{-0.5}$ . This may suggest that  $\lambda_q$  is connected to global plasma parameters; however, the fact that critical gradient models for core transport also depend on pedestal top parameters can introduce a correlation between edge and core (and, thus, between edge and global plasma parameters). This can mask the actual physically relevant dependence of  $\lambda_q$  on local edge plasma parameters. In order to disentangle the effect of local and global parameters on  $\lambda_q$ , it is of interest to investigate plasma discharges with similar global parameters and different pedestal top values.

The present work reports on power decay length correlation studies across different confinement regimes present at ASDEX Upgrade (AUG), namely L-mode, I-mode, inter-ELM H-mode and the recently achieved stationary ELM-free H-mode [12]. Three main questions will be addressed throughout this paper: (1) Is a cross-regime  $\lambda_q$  scaling better described by global or local edge plasma parameters? (2) Is there a connection between SOL and pedestal gradients? (3) How are upstream (outer midplane) SOL decay lengths correlated to  $\lambda_q$  across different confinement regimes?

To answer the first question, we analyze a wide range of discharges that allows us to break the correlation between global and edge plasma parameters. In all these discharges, the heat flux profile onto the divertor targets is inferred from infrared cameras measurements [13]. Indeed, it is shown that  $\lambda_q$  exhibits a clear correlation with a local edge plasma parameter (the electron pressure measured at  $\rho_{\text{pol}} = 0.95$ ) across all confinement regimes, while it shows a more scattered correlation with global quantities such as the volume-averaged core plasma pressure or the average poloidal magnetic field.

To answer the second and third questions, the divertor database is enriched with near-SOL electron pressure, temperature and density decay lengths ( $\lambda_{p_e}^{\text{SOL}}$ ,  $\lambda_{T_e}^{\text{SOL}}$  and  $\lambda_{n_e}^{\text{SOL}}$ , respectively) estimated from the edge Thomson scattering system [14] installed at AUG. To the knowledge of the authors, for the first time this allowed us to build a cross-regime (L, I and H-mode)  $\lambda_q$  and  $\lambda_{T_e, n_e, p_e}^{\text{SOL}}$  database. In agreement with earlier studies [15–17], it is shown that the relation

$\lambda_q = \frac{2}{7} \lambda_{T_e}^{\text{SOL}}$  describes the correlation between  $\lambda_q$  at the divertor and  $\lambda_{T_e}^{\text{SOL}}$  at the outer midplane well across all confinement regimes analyzed, which are all in attached divertor conditions. On the other hand, a larger scatter is found when  $\lambda_q$  is plotted against  $\lambda_{n_e}^{\text{SOL}}$ , suggesting a weaker role of  $\lambda_{n_e}^{\text{SOL}}$  in setting  $\lambda_q$ . Lastly, evidence of a strong correlation between SOL and pedestal electron pressure gradients across all confinement regimes is shown. The physical interpretation of this observation is discussed, in particular, with regard to a critical edge pressure gradient paradigm governing the edge physics [18, 19] and to a turbulence spreading model for the SOL [20, 21].

The paper is organized as follows: In section 2, the database is described. In section 3, the key diagnostics and the evaluation method are shown. The scaling of  $\lambda_q$  with global and local edge quantities is outlined in section 4, whereas correlations between SOL and pedestal gradients are shown in section 5. In section 6, the relation between upstream SOL decay lengths and  $\lambda_q$  is discussed. Considerations of the presented results are exposed in section 7 and, finally, in section 8, the main conclusions are drawn.

## 2. Database

ASDEX Upgrade is a medium-size divertor tokamak [22] that can perform discharges both in lower single null (LSN) and in upper single null (USN) plasma configurations. The closed lower outer divertor (vertical target) is composed of bulk tungsten tiles inclined in the toroidal direction to prevent leading edge formation. Therefore, the lower divertor is optimized for one magnetic field direction. On the other hand, the open upper divertor (horizontal target) is composed of tungsten-coated graphite tiles that are not toroidally tilted, allowing thus more flexibility in the magnetic field direction. At AUG, L-mode and H-mode confinement regimes are regularly achieved in both LSN and USN configurations. However, the I-mode [23, 24] needs a higher H-mode power threshold to be accessed. This is usually achieved by using magnetic configurations with the ion  $\nabla B$  drift pointing away from the active X-point, i.e. the so-called unfavorable configuration in terms of H-mode access. Plasma discharges in the unfavorable configuration can be achieved in both the LSN and USN configuration at AUG. However, in LSN, both the toroidal magnetic field and the plasma current need to be reversed in order to keep the same magnetic field line inclination at the divertor tiles to avoid leading edges. On the contrary, USN plasmas in unfavorable configuration are achieved without reversing the plasma current direction, as the divertor tiles are not optimized for one magnetic field line inclination. Since reversing the plasma current limits the usage of the NBI heating system due to strong ion orbit losses, plasmas in the unfavorable configuration—and thus I-modes as well—are more frequently studied in USN at AUG. Therefore, in this work, I-mode discharges are all in USN configuration, while L-mode and H-mode discharges are

**Table 1.** Parameter range of the ASDEX Upgrade discharges analyzed.

	L-mode	I-mode	Type-I-ELM H-mode	ELM-free H-mode
	USN/LSN	USN	USN/LSN	LSN
Configuration Discharges	20	22	5	2
$\tau_E$ (ms)	32–192	38–140	53–213	180–210
$W_{\text{MHD}}$ (kJ)	68–310	204–394	259–611	270–300
$\beta_{\text{pol}}$	0.2–1.1	0.4–1.2	0.6–1.0	0.7
$H_{98y,2}$	0.5–0.9	0.7–0.9	0.8–1.3	0.9–1.0
$P_{\text{heat}}$ (MW)	0.5–4.2	2.1–4.2	1.4–6.6	1.4–1.7
$P_{\text{sep}}$ (MW)	0.2–2.6	1.7–2.8	0.5–3.7	0.5–0.8
$n_e$ ( $10^{19} \text{ m}^{-3}$ )	1.4–5.5	2.4–6.0	4.9–9.4	7.8–8.4
$I_p$ (MA)	0.6–1	0.6–1	0.8–1	0.8
$\langle B_{\text{pol}} \rangle$ (T)	0.2–0.4	0.2–0.4	0.3–0.4	0.3
$B_t$ (T)	2.5	1.8–3	2.5	2.5
$\delta$	0.1–0.4	0.2–0.3	0.1–0.4	0.3

present in both LSN and USN configurations. This allowed us to study L-mode and H-mode plasmas with both ion  $\nabla B$  drift directions (pointing to and away from the active X-point) and with different divertor geometries (closed lower divertor versus open upper divertor). LSN L-mode discharges described in [25] are reexamined here. H-mode data were taken between type-I-ELMs (both in LSN and USN configurations) and in stationary ELM-free plasmas [12] recently achieved at AUG (only in LSN). The database consists of 34 discharges, among which 12 are in LSN, while 22 are in USN. 16 discharges exhibit both L-mode and I-mode plasmas. To guarantee high-quality IR measurements, discharges with impurity seeding and divertor detachment have not been considered. Only deuterium discharges are considered in this study.

Table 1 shows the parameter range covered in the database. The energy confinement time is denoted  $\tau_E$ ,  $W_{\text{MHD}}$  is the plasma stored energy determined from the reconstructed magnetic equilibrium,  $\beta_{\text{pol}}$  is the poloidal beta,  $H_{98y,2}$  is the energy confinement time normalized to the IPB98(y,2) scaling law [26],  $P_{\text{heat}}$  is the heating power,  $P_{\text{sep}}$  is the power crossing the separatrix given by  $P_{\text{sep}} = P_{\text{heat}} - dW/dt - P_{\text{rad}}$ , where  $W$  is the total plasma energy and  $P_{\text{rad}}$  is the power radiated within the separatrix,  $n_e$  is the line averaged electron density measured by the DCN interferometer channel H-1, which crosses the plasma core [27],  $I_p$  is the plasma current,  $B_t$  is the toroidal magnetic field at the magnetic axis,  $\delta$  is the plasma triangularity and  $\langle B_{\text{pol}} \rangle$  is the average poloidal magnetic field defined as

$$\langle B_{\text{pol}} \rangle = \frac{\mu_0 I_p}{2\pi a \sqrt{\frac{1+\kappa^2}{2}}} = \frac{\mu_0 I_p}{2\pi a \hat{\kappa}}, \quad (1)$$

where  $a$  is the minor radius,  $\kappa$  is the elongation of the plasma and  $\hat{\kappa} = \sqrt{\frac{1+\kappa^2}{2}}$ .

### 3. Diagnostics and analysis technique

In this work, the most important measured quantities are (i) the heat flux reaching the divertor targets, (ii) the scrape-off layer (SOL) electron pressure, temperature and density decay lengths and (iii) the electron pressure profile in the confined region of the plasma. The heat flux onto the divertor targets is inferred from surface temperature measurements obtained with infrared (IR) cameras [13] installed on the low field side of AUG. The lower outer divertor is observed with a tangential view, whereas the upper divertor targets are monitored using a poloidal view through a periscope. Both IR cameras measure around a wavelength of  $4.7 \mu\text{m}$ . The spatial resolution for the lower outer target is  $0.6 \text{ mm/pixel}$ , while for the upper outer (inner) target it is  $2.3 \text{ mm/pixel}$  ( $1.5 \text{ mm/pixel}$ ). The different spatial resolution for the upper outer and inner target is due to the viewing angle of the camera looking at the upper divertor. The flux expansion  $f_x$  between the outer midplane and the lower outer, upper outer and upper inner targets is about 6, 7, and 9.5, respectively. Therefore, the spatial resolution at the outer midplane is  $\approx 0.1$ ,  $0.3$  and  $0.15 \text{ mm}$ , respectively. The camera frame rate is between 400 and 2130 Hz. These sampling frequencies are sufficient to resolve inter-ELM phases, as the ELM frequency of the analyzed H-mode discharges ranges between 10 and 70 Hz. IR cameras measure the divertor target surface temperature from which the heat flux is calculated using the implicit version [28] of the THEODOR code [29]. Figure 1(e) shows an example of a heat flux profile measured at the upper outer divertor target. Data are fitted with the function [30]:

$$q(\bar{s}) = \frac{q_0}{2} \exp \left[ \left( \frac{S}{2\lambda_q} \right)^2 - \frac{\bar{s}}{\lambda_q f_x} \right] \text{erfc} \left( \frac{S}{2\lambda_q} - \frac{\bar{s}}{S f_x} \right) + q_{\text{BG}}. \quad (2)$$

where  $\bar{s} = s - s_0$  is the location on target with the origin at the strike line location  $s_0$ ,  $\lambda_q$  is the power decay length mapped to the outer midplane via the flux expansion  $f_x$ ,  $S$  is the power broadening also mapped to the outer midplane and  $q_{\text{BG}}$  is a background heat flux. In order to evaluate  $\lambda_q$  and  $S$  within a certain time window  $\Delta t$  (about 50 ms), the following method is carried out: First, the fitting function is applied to each heat flux profile within the time interval  $\Delta t$ . Second, only pairs of  $\lambda_q$  and  $S$  satisfying the condition  $\lambda_q/S \geq 1.5$  are taken into account. This condition is chosen because when  $\lambda_q \simeq S$ , the  $\lambda_q$  measured at the divertor target is strongly influenced by the Gaussian broadening taking place in the divertor chamber. Lastly, the median of all the  $\lambda_q$  (and  $S$ ) values within the time window is calculated. An example of the  $\lambda_q$  and  $S$  time evolutions calculated with the aforementioned method are shown in figures 1(a) and (b). Other important plasma parameters used in this work are the SOL electron pressure, temperature and density decay lengths. SOL profiles are routinely measured by a vertical Thomson Scattering (TS) system [14] with a time resolution of 120 Hz, from which SOL electron temperature and density decay lengths  $\lambda_{T_e}^{\text{SOL}}$  and  $\lambda_{n_e}^{\text{SOL}}$  can be calculated. From here on, the subscript ‘SOL’ is omitted for reading purposes and it will be



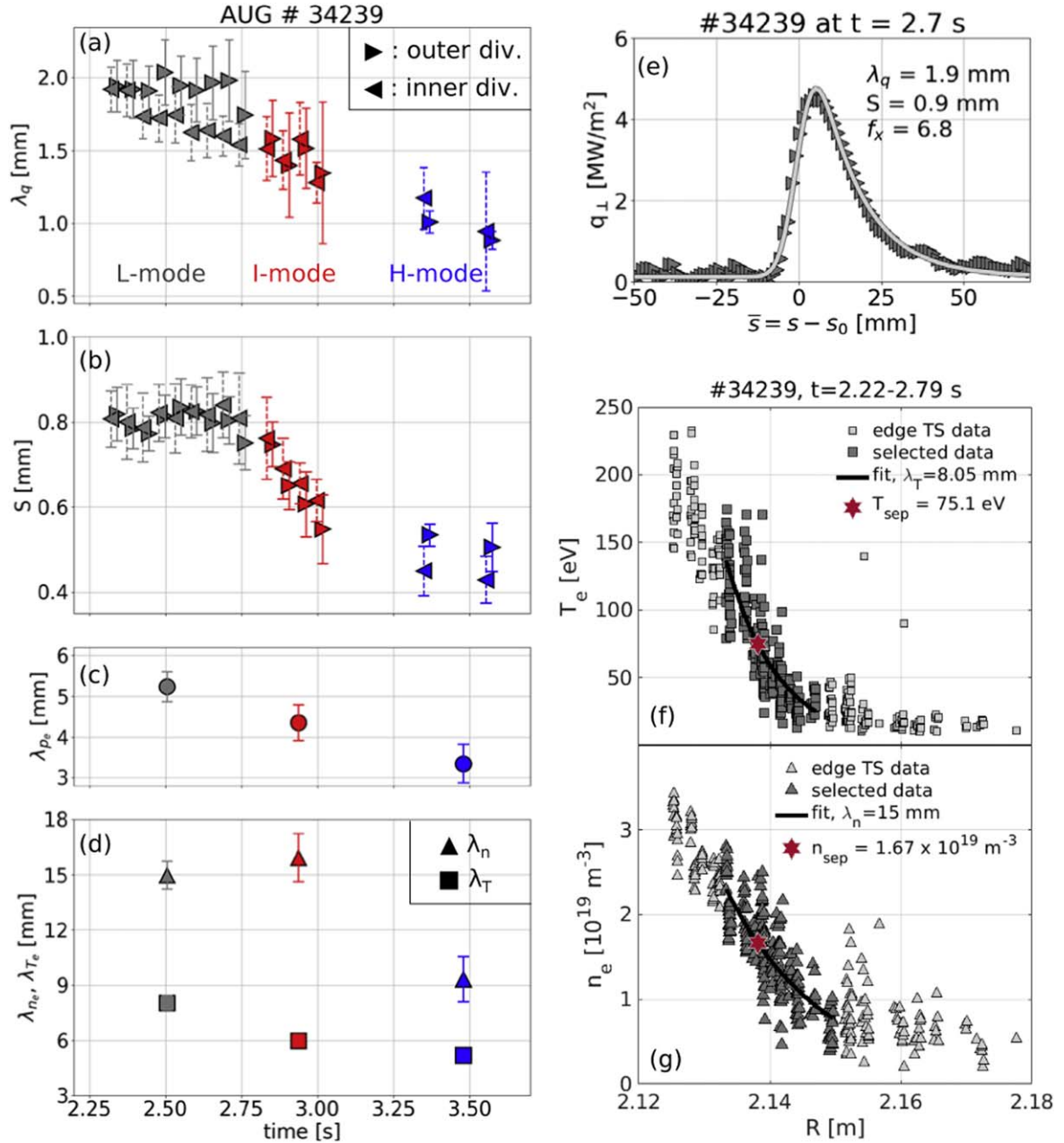


**Figure 1.** Temporal evolution of SOL and divertor parameters along discharge #34239 exhibiting different confinement regimes. Power fall-off length (a) and broadening (b) obtained from inner ( $\blacktriangleleft$  with dashed error bars) and outer ( $\blacktriangleright$  with line error bars) divertor heat fluxes. L-mode, I-mode and H-mode phases are represented in gray, red and blue, respectively. (c) Electron pressure near-SOL decay length. (d) Near-SOL decay lengths of electron density (triangles) and temperature (squares). Panel (e) shows the perpendicular heat flux profile along the upper outer divertor and its fit with equation (2). Panels (f) and (g) show, respectively, edge electron temperature and density profiles measured by Thomson Scattering (TS). Data selected for the exponential fit are depicted in dark gray. The red stars represent the separatrix electron temperature and density.

used only when necessary. The separatrix position is evaluated following the model used in [31], where the electron temperature at the separatrix is given by:

$$T_e^{\text{sep}} = \left( \frac{7}{4} \frac{P_{\text{sep}} L_c}{\kappa_0^e A_{\text{SOL}}} \right)^{\frac{2}{7}}, \quad (3)$$

where  $L_c \simeq \pi q_{\text{cyl}} R$  is the connection length from the outer midplane to the divertor target,  $A_{\text{SOL}}$  is the cross-sectional area of the SOL perpendicular to the magnetic field lines and

$\kappa_0^e \simeq 2000 \text{ (eV)}^{7/2} \text{ Wm}^{-1}$  is the Spitzer–Härm conductivity constant for electrons. By writing  $A_{\text{SOL}} = 4\pi R \langle \lambda_q \rangle \frac{B_{\text{pol}}}{B_{\text{tor}}}$ , with  $\langle \lambda_q \rangle$  being the poloidally averaged  $\lambda_q$  ( $\lambda_q \simeq 0.56 \langle \lambda_q \rangle$  for typical AUG geometries [30]), and by using  $q_{\text{cyl}} = \frac{B_{\text{tor}} \hat{r}}{\langle B_{\text{pol}} \rangle A}$  and  $A = R/a$ , we rewrite equation (3) as:

$$T_e^{\text{sep}} \approx \left( \frac{7}{16} \frac{P_{\text{sep}} q_{\text{cyl}}^2 A}{\kappa_0^e \hat{r} \langle \lambda_q \rangle} \right)^{\frac{2}{7}}. \quad (4)$$

The separatrix temperature is evaluated with equation (4) using  $\lambda_q$  from IR measurements. Once  $T_e^{\text{sep}}$  is known, the separatrix position ( $r_{\text{sep}}$ ) can be estimated and a subset of selected data (between  $r_{\text{sep}} - 5$  mm and  $r_{\text{sep}} + 9$  mm) is fitted with an exponential, i.e.  $T_e(r) = T_e^{\text{sep}} \exp\left(-\frac{r-r_{\text{sep}}}{\lambda_{T_e}}\right)$ , to find the SOL electron temperature decay length  $\lambda_{T_e}$ . A similar approach is used to evaluate the SOL electron density decay length  $\lambda_{n_e}$ . In order to have a more robust ensemble of datapoints to minimize fitting errors, several TS profiles within a long time window (about 300 ms) are collected before carrying out the fit. Figures 1(f) and (g) show an example of edge electron temperature and density profiles mapped to the outer midplane. Once the SOL  $\lambda_{T_e}$  and  $\lambda_{n_e}$  are known, the electron pressure decay length is obtained using the relation

$$1/\lambda_{p_e} = 1/\lambda_{T_e} + 1/\lambda_{n_e}. \quad (5)$$

At AUG, electron temperature, density and pressure profiles within the confined region of the plasma are evaluated through integrated data analysis (IDA) [32], which combines different diagnostics such as electron cyclotron emission, lithium beam emission spectroscopy, DCN interferometry and Thomson scattering. This allows us to obtain more accurate profiles with reduced uncertainties. IDA profiles will be used in this work to evaluate electron temperature, density and pressure values at  $\rho_{\text{pol}} = 0.95$ . Figure 1 shows an example of how SOL and divertor quantities evolve together along a discharge characterized by L-mode, I-mode and type-I-ELMy H-mode phases. Panels (a) and (b) show  $\lambda_q$  and  $S$ , respectively, measured at the inner ( $\blacktriangleleft$ ) and outer ( $\blacktriangleright$ ) upper divertor target and then mapped to the outer midplane. As already shown in [17],  $\lambda_q$  gradually decreases when passing from L to I-mode and it is reduced even more after the I–H transition. Note that H-mode  $\lambda_q$  values are about a factor of 1.8 smaller than those predicted by the scaling law in [30], which was obtained in a carbon wall environment. Further studies to address the dependency of  $\lambda_q$  on such plasma conditions are envisaged at AUG. During the L-mode inner and outer divertor  $\lambda_q$  values show a small discrepancy, with  $\lambda_q^{\text{out}} > \lambda_q^{\text{inn}}$ , as already found in [16]. The observed asymmetry could be due to the vertical magnetic drifts of ions and the plasma triangularity [5, 16, 25]. The broadening parameter  $S$  does not show any large asymmetry between inner and outer divertors across all confinement regimes, extending to I-mode and H-mode what has been already observed in USN L-mode discharges [16]. The variation of  $S$  along the three confinement regimes is reminiscent of the  $\lambda_q$  change: It stays roughly constant during the L-mode phase, then it decreases during the I-mode and eventually remains constant at low values during the H-mode. The SOL electron pressure decay length evolution, panel (c), closely resembles the  $\lambda_q$  evolution, exhibiting a constant gradual decrease going from L to I-mode and from I to H-mode. Likewise,  $\lambda_{T_e}$  (squares in panel (d)) shows a similar behavior to  $\lambda_{p_e}$ , even though its reduction passing from I to H-mode is less marked. On the other hand,  $\lambda_{n_e}$  (triangles in panel (d)) evolves differently: it stays roughly constant passing from L to I-mode, whereas it drops only after

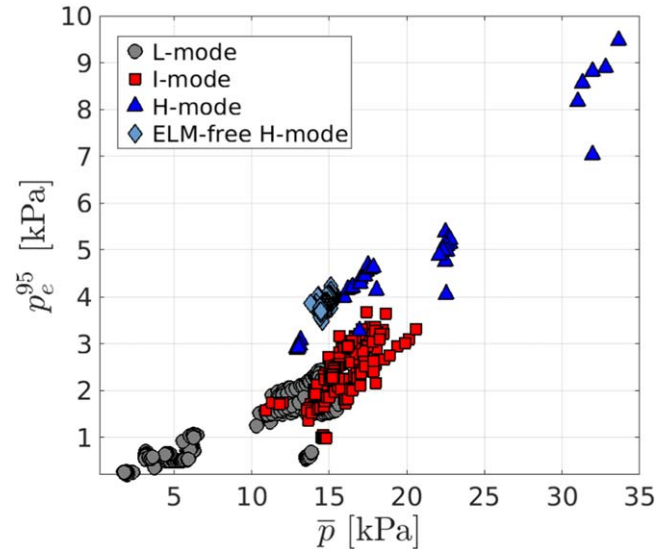


**Figure 2.** Edge electron pressure evaluated at  $\rho_{\text{pol}} = 0.95$  against volume-averaged plasma pressure. The database allows us to break the dependence between global and local (edge) pressure quantities.

the I–H transition [17]. In the following, error bars will be omitted for visibility purposes. The relative error of  $\lambda_{T_e}$  and  $\lambda_{n_e}$  ranges between 5% and 15%, while the one of  $\lambda_q$  varies approximately between 5% and 30%.

#### 4. Cross-regime scaling of the power decay length $\lambda_q$

One of the main goals of this study is to investigate whether a cross-regime  $\lambda_q$  scaling is better described by global or local edge plasma parameters. Figure 2 illustrates the relation between the edge electron pressure evaluated at  $\rho_{\text{pol}} = 0.95$  ( $p_e^{0.95}$ , which is the pedestal top electron pressure in I-mode and H-mode) and the volume-averaged plasma pressure defined as  $\bar{p} = \frac{2}{3} W_{\text{MHD}} / V$ , where  $V$  is the plasma volume. Due to some H-mode data and few L and I-mode data outliers, the database used in this work allows us to disentangle the dependency between volume-averaged and edge plasma parameters. From here on, different confinement regimes will be depicted with the color and symbol code used in figure 2. Figure 3 shows the relation between the average poloidal magnetic field and  $\lambda_q$ . For the same  $\langle B_{\text{pol}} \rangle$ ,  $\lambda_q$  can assume different values depending on the confinement regime. In particular, for  $\langle B_{\text{pol}} \rangle = 0.31$  T,  $\lambda_q \in [0.8, 4.5]$  mm, spanning from L to H-mode. This is in accordance with different pre-factors in front of H-mode and L-mode  $\lambda_q$  scaling laws [11, 25, 30].

Figure 4(a) shows the SOL power fall-off length against the volume-averaged plasma pressure  $\bar{p}$ . Note that the definition of  $\bar{p}$  is equivalent to the one used for the C-Mod studies in [11], which led to the scaling  $\lambda_q [\text{mm}] = 0.91 (\bar{p} [\text{atm}])^{-0.48}$  (or equivalently  $\lambda_q [\text{mm}] = 8.35 (\bar{p} [\text{kPa}])^{-0.48}$ ). A nonlinear regression of the form  $\lambda_q = C \times \bar{p}^\alpha$  is carried out and the result is shown in figure 4(a) as a light green line.  $\lambda_q$  shows a correlation with  $\bar{p}$  ( $R^2 = 0.62$ ) with a similar exponent and coefficient as in the C-Mod scaling (at AUG  $\alpha = -0.52$  and

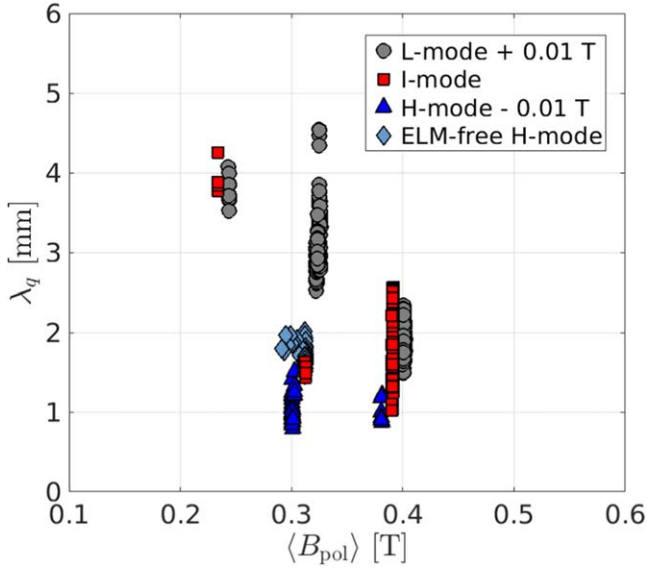


**Figure 3.** SOL power decay length  $\lambda_q$  against the average poloidal magnetic field. L-mode (H-mode)  $\langle B_{\text{pol}} \rangle$  values are shifted by + (−) 0.01 T for visibility purposes. At a fixed  $\langle B_{\text{pol}} \rangle$ ,  $\lambda_q$  spans over a broad range of values depending on the confinement regime.

$C = 7.57$ ). However, for a volume-averaged plasma pressure of 15 kPa,  $\lambda_q$  shows a large scatter in the range 0.9–4 mm. Figure 4(b) shows the relation between  $\lambda_q$  and the edge electron pressure,  $p_e^{95}$ . A nonlinear regression yields ( $R^2 = 0.77$ ):

$$\lambda_q [\text{mm}] = 2.45 \pm 0.02 \times (p_e^{95} [\text{kPa}])^{-0.34 \pm 0.01}. \quad (6)$$

The regression describes L-mode, I-mode and stationary ELM-free H-mode data well, while representing an upper boundary for inter-type-I ELM H-mode data. A conservative scaling for the inter-type-I ELM H-mode data is given by halving the regression coefficient. Overall, this regression is broadly consistent with the scaling found at Alcator C-Mod, since all data from different confinement regimes correlate well with one plasma parameter related to the plasma pressure; however, at AUG the edge electron pressure is found to be a more suitable parameter for a  $\lambda_q$  scaling than a volume-averaged plasma quantity, such as  $\bar{p}$ . Indeed, as an edge local plasma parameter,  $p_e^{95}$  should be more related to the SOL physics setting  $\lambda_q$  than a global quantity such as  $\bar{p}$ . This consideration is also supported by recent HESEL simulations, which show that simulated L-mode  $\lambda_q$  values scale remarkably well with the electron (and ion) pressure gradient across the separatrix [33]. It should be also noted that the present scaling law has been obtained with discharges characterized by attached divertor conditions and no impurity seeding. However, within these two operational constraints (which were necessary to guarantee high-quality heat flux measurements), plasma conditions were strongly varied. The database contains not only a large variety of pedestal profiles, but also L-mode and H-mode discharges with different ion  $\nabla B$  drift directions and different divertor geometries. Therefore, it is important to notice the generality of this scaling, which may highlight a possible unified physics mechanism setting  $\lambda_q$  across different confinement regimes.

Table 2 summarizes the results of nonlinear regressions of the form  $\lambda_q = C \times X^\alpha$  applied to different parameters. In particular, the low  $R^2$  value obtained when  $T_e^{95}$  is used in the nonlinear regression ( $R^2 = 0.29$ ) should be noted, in contrast to the high values obtained with  $p_e^{95}$  ( $R^2 = 0.77$ ) and  $n_e^{95}$  ( $R^2 = 0.71$ ). Therefore, the edge electron temperature is found to be a weak parameter for describing a cross-regime  $\lambda_q$  scaling, in contrast to what has been found when analyzing L-mode data alone [25, 34].

## 5. On the connection between SOL and pedestal electron pressure gradients

To further investigate the reasons for the  $\lambda_q$  correlation with  $p_e^{95}$ , figure 5 shows the relation between  $\lambda_q$  and two edge electron pressure quantities: the SOL electron pressure decay length at the outer midplane  $\lambda_{p_e}^{\text{SOL}}$  (panel (a)), which has been calculated with equation (5), and the pedestal electron pressure gradient length  $L_{p_e}^{\text{ped}}$  (panel (b)). If the pedestal profile is best described by a straight line, as suggested in [35],  $L_{p_e}^{\text{ped}}$  can be simply estimated by:

$$L_{p_e}^{\text{ped}} = -\frac{p_e}{\nabla p_e} \approx \frac{p_e^{95} + p_e^{\text{sep}}}{2} \cdot \frac{R^{\text{sep}} - R^{95}}{p_e^{95} - p_e^{\text{sep}}}, \quad (7)$$

where the subscripts ‘sep’ and ‘95’ denote values taken at the separatrix and  $\rho_{\text{pol}} = 0.95$ , respectively. Both  $p_e^{\text{sep}}$  and  $R_{\text{sep}}$  are calculated with the method described in section 3.

A clear correlation can be noted between  $\lambda_q$  and both  $\lambda_{p_e}^{\text{SOL}}$  and  $L_{p_e}^{\text{ped}}$ , in particular,  $\lambda_q$  rises with  $\lambda_{p_e}^{\text{SOL}}$  or  $L_{p_e}^{\text{ped}}$  increases. Also, the correlations show a similar trend: a certain value is observed ( $\lambda_{p_e}^{\text{SOL}} \simeq 5.5$  mm and  $L_{p_e}^{\text{ped}} \simeq 19$  mm), after which  $\lambda_q$  increases more strongly. This change coincides with the transition from I to L-mode and could reflect the larger radial turbulent transport usually found at the edge of L-mode plasmas. Also, it is worth noting the different absolute values of the pedestal and SOL gradient lengths, with the SOL one being steeper than the pedestal one. This observation is in accordance with what was previously found at Alcator C-Mod [18] and with 2D-fluid edge simulations [36], namely that the electron pressure gradient exhibits a minimum in the near-SOL. However, the larger values of pedestal gradient lengths, w.r.t. the SOL, may be also partially explained by the approximate estimation of the pedestal top position, which is here assumed to be at  $\rho_{\text{pol}} = 0.95$ . Nonetheless, what should be retained from figure 5 is that the steepening of edge pressure profiles (i.e. an increase of pedestal and core pressures) is statistically associated with a reduction of  $\lambda_q$ . Note that this relation is not valid for only one confinement regime, but it is present across all regimes analyzed.

This consideration may have important consequences for next step devices, since the ultimate goal of a fusion power plant is to combine high core plasma pressure (which means steep pedestal pressure gradients, as core profiles are mainly stiff) with a good enough power exhaust solution, which

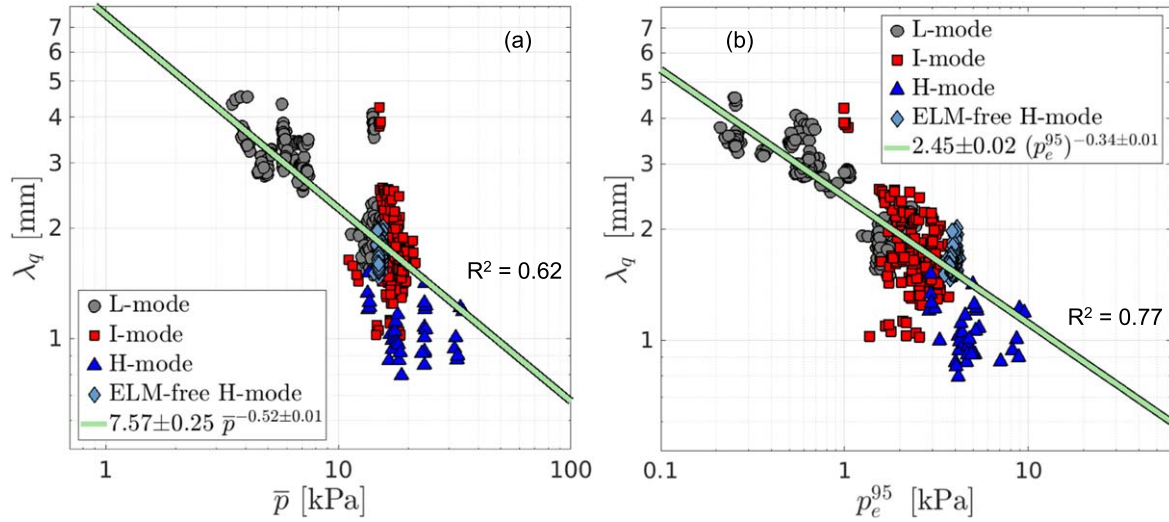


**Figure 4.** Power decay length  $\lambda_q$  against (a) the volume-averaged plasma pressure  $\bar{p}$  and (b) edge electron pressure evaluated at  $\rho_{\text{pol}} = 0.95$ ,  $p_e^{95}$ . Light green lines represent the results of a nonlinear regression of the form  $\lambda_q = C \times X^\alpha$ . The respective  $R^2$  values are shown in the picture.

**Table 2.** Overview of selected regression results.

#	C	$p_e^{95}$ [kPa]	$\bar{p}$ [kPa]	$T_e^{95}$ [keV]	$n_e^{95}$ [ $10^{19} \text{ m}^{-3}$ ]	$\langle B_{\text{pol}} \rangle$ [T]	$R^2$
1	2.45	-0.34	—	—	—	—	0.77
2	7.57	—	-0.52	—	—	—	0.62
3	0.95	—	—	-0.67	—	—	0.29
4	3.37	—	—	—	-0.43	—	0.71
5	0.55	—	—	—	—	-1.23	0.19

largely depends on  $\lambda_q$  [2–4]. In addition, it is interesting to notice that the correlation between  $\lambda_q$  and  $L_p^{\text{ped}}$  is broken by few I-mode outliers. The I-mode plasma with  $\lambda_q \approx 4$  mm is the burst-dominated I-mode shown in [17]. In such discharges, filamentary transport is suspected to broaden the SOL width and, interestingly, the pressure pedestal gradient length stays at the same typical I-mode values. This case is adding up to other recent findings at AUG that show a widening of the SOL temperature decay length in high-density H-mode discharges [15, 37].

Figure 6 shows the relation between the pedestal and SOL electron pressure gradients ( $1/L_p^{\text{ped}}$  and  $1/\lambda_p^{\text{SOL}}$ , respectively), here normalized to the AUG major radius  $R = 1.65$  m. Remarkably, SOL and pedestal gradients appear to be linearly correlated across all confinement regimes, namely an increase of  $R/\lambda_p^{\text{SOL}}$  corresponds to an according increase of  $R/L_p^{\text{ped}}$ . To quantify their relationship, a linear fit is applied to the data yielding ( $R^2 = 0.83$ )

$$\frac{R}{L_p^{\text{ped}}} = 39.4 + 0.2 \cdot \frac{R}{\lambda_p^{\text{SOL}}}. \quad (8)$$

Data are all contained within the 15% error boundaries plotted in figure 6 as black dashed lines. The reasons for the existence of an offset are unclear at this stage.

## 6. Upstream SOL decay lengths across different confinement regimes

In this section, the relationship between experimental  $\lambda_q$ ,  $\lambda_{T_e}$  and  $\lambda_{n_e}$  is studied across different confinement regimes. As already shown in figure 1(d) and in [17, 38], SOL electron temperature and density decay lengths behave differently in L-mode, I-mode and H-mode discharges. Figure 7(a) shows the relation between electron temperature  $\lambda_{T_e}$  and density  $\lambda_{n_e}$  decay lengths across all analyzed confinement regimes. H-mode discharges (both ELMy and stationary ELM-free H-mode) are characterized by short temperature and density SOL decay lengths, whereas L-mode discharges are usually characterized by long temperature and density SOL decay lengths. The well-heated L-mode discharges (i.e. close to the L-H transition), however, can feature short temperature decay lengths, similar to those of marginally-heated H-mode discharges (i.e. close to the L-H transition), such as stationary ELM-free H-mode discharges. On the other hand, I-mode discharges are characterized by small  $\lambda_{T_e}$  and large  $\lambda_{n_e}$  values. This general behavior is reminiscent of the electron temperature and density pedestal evolution across the different confinement regimes. In figure 7(a), two lines representing different gradient length ratios  $\eta_e = \lambda_{n_e}/\lambda_{T_e} = 1$  and  $\eta_e = 2$  are depicted. L-mode and H-mode discharges are characterized by  $1 \leq \eta_e \leq 2$ . This is in line with previous studies



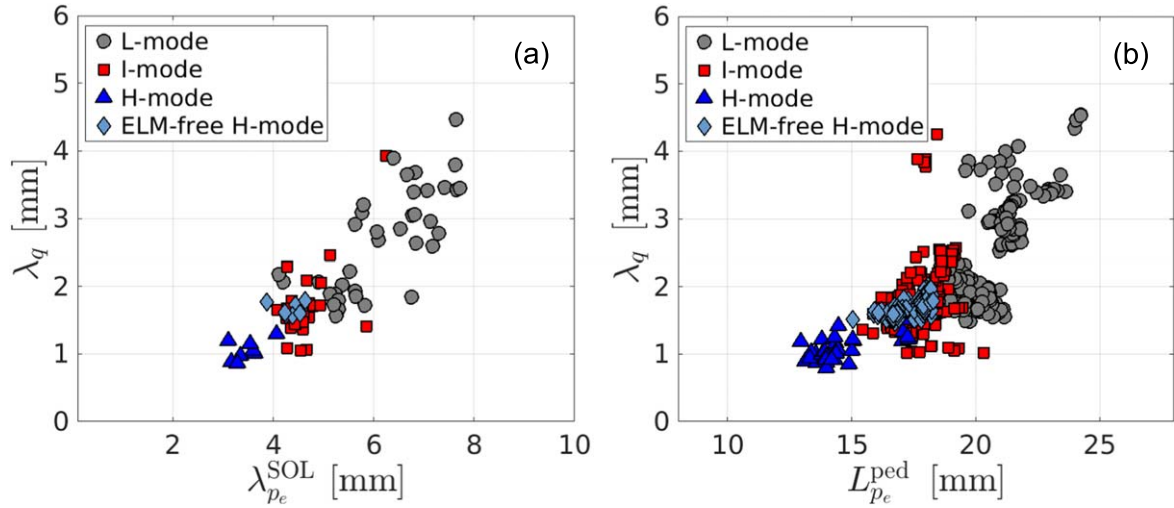


**Figure 5.** SOL power decay length  $\lambda_q$  against (a) SOL electron pressure decay length and (b) pedestal electron pressure gradient length,  $L_{p_e}^{\text{ped}}$ . L-modes, I-modes, inter-ELM H-modes and stationary ELM-free H-modes are represented in gray circles, red squares, blue triangles and light blue diamonds, respectively.

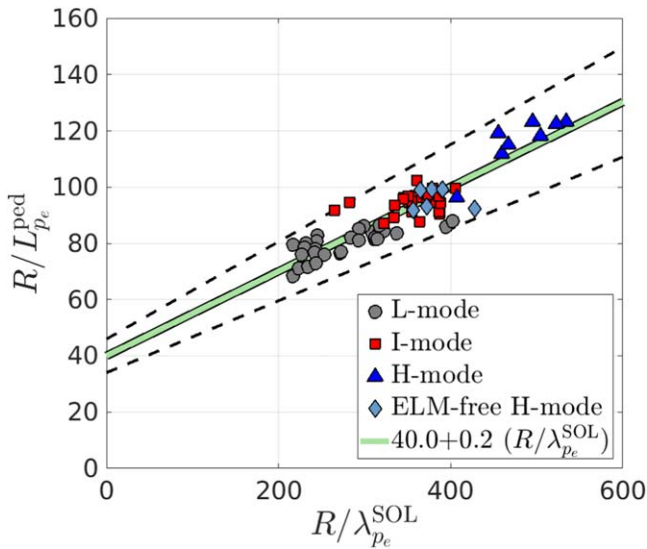


**Figure 6.** Normalized pedestal electron pressure gradient against the normalized SOL electron pressure gradient. The result of a linear fit is depicted as a green line. Dashed black lines represent the 15% error boundaries that encompass all data. Remarkably, SOL and pedestal electron pressure gradients are correlated across all confinement regimes.

conducted at AUG for the type-I-ELMy H-mode regime [15]; however, I-mode discharges are characterized by  $\eta_e \geq 2$ , due to their H-mode-like  $\lambda_{T_e}$  (about 7 mm) and L-mode-like  $\lambda_{n_e}$  (around 15 mm). This is highlighting the decoupling of SOL electron density and temperature decay lengths that occurs in I-mode plasmas. Figure 7(b) shows the relation between  $\lambda_{p_e}$  and  $\lambda_{T_e}$ , which are linked through  $1/\lambda_{p_e} = 1/\lambda_{T_e} + 1/\lambda_{n_e}$ . Substituting  $\eta_e = 1$  and  $\eta_e = 2$  in the previous formula, one can find the corresponding relations between SOL electron pressure and temperature decay lengths, which are  $\lambda_{p_e} = \frac{1}{2} \lambda_{T_e}$  and  $\lambda_{p_e} = \frac{2}{3} \lambda_{T_e}$ , respectively. As expected, most of the dataset lies between those two lines except for the I-mode

discharges, which have  $\eta_e > 2$ . What should be retained from this graph is that  $\lambda_{p_e}$  and  $\lambda_{T_e}$  remain interconnected, even though I-mode discharges have allowed us to enlarge the dataset in the  $\lambda_{n_e}$ - $\lambda_{T_e}$  diagram. For this reason, disentangling  $\lambda_{T_e}$  and  $\lambda_{p_e}$  dependencies with the present database remains challenging. Nevertheless, the variety of combinations of density and temperature SOL decay lengths, obtained thanks to the cross-regime analysis, allows us to study their single effect on  $\lambda_q$ . Figure 8(a) shows the relation between experimentally measured  $\lambda_q$  and the electron temperature SOL decay length  $\lambda_{T_e}$  across different confinement regimes at AUG. If in the SOL most of the parallel heat transport is due to electron conduction,  $\lambda_q$  and  $\lambda_{T_e}$  are related by the formula  $\lambda_q = \frac{2}{7} \lambda_{T_e}$  [31]. Previous studies at AUG have shown that this relation holds in L-mode [16], in a single I-mode discharge [17] and H-mode discharges [15] (in the last case  $\lambda_{T_e}$  was compared with  $\lambda_q$  estimated by scaling laws). Figure 8(a) shows that all data cluster around the line  $\lambda_q = \frac{2}{7} \lambda_{T_e}$  across all different confinement regimes. Therefore, it can be concluded that at ASDEX Upgrade the Spitzer–Härm electron heat conduction assumption gives a reasonable connection between  $\lambda_{T_e}$  measured upstream and  $\lambda_q$  measured at the target. Figure 8(b) shows the relation between  $\lambda_q$  and  $\lambda_{n_e}$  across the different confinement regime analyzed. For  $\lambda_q \approx 1.5$  mm,  $\lambda_{n_e}$  ranges between 7 and 20 mm; On the other hand, for  $\lambda_{n_e} \approx 17$  mm,  $\lambda_q$  shows a large variation from 1 mm to about 4.5 mm. This plot suggests a weaker role of the SOL electron density decay length in setting  $\lambda_q$ , when compared to that of  $\lambda_{T_e}$ .

## 7. Discussion

Results from the present study highlight a correlation between SOL and pedestal electron pressure gradients that holds across all analyzed confinement regimes (figure 6). This finding allows us to address two main points:

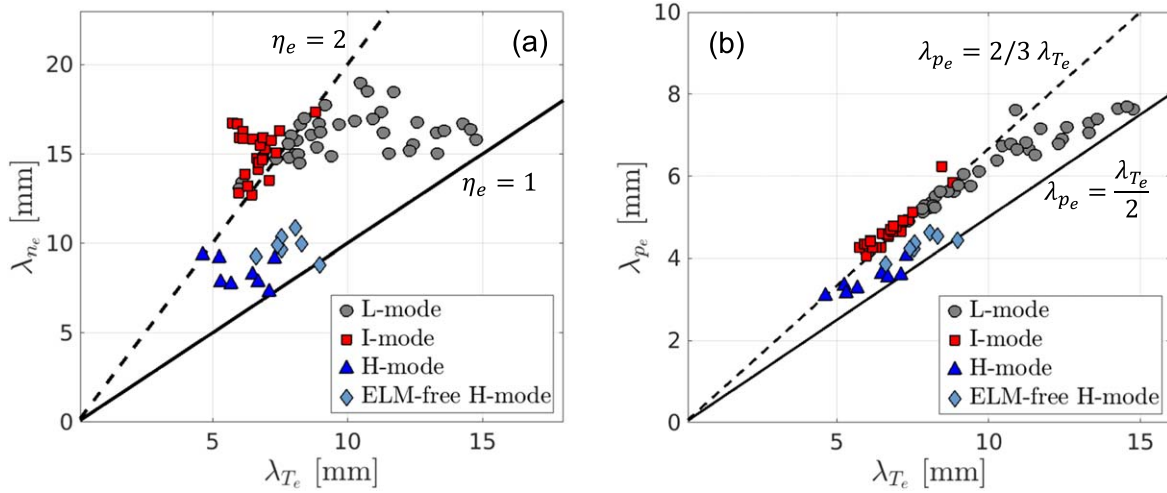


**Figure 7.** SOL electron density decay length (a) and SOL electron pressure decay length (b) against SOL electron temperature decay length across different confinement regimes. In panel (a) dashed and solid lines represent  $\eta_e = 2$  and  $\eta_e = 1$ , respectively, with  $\eta_e = \lambda_{n_e}/\lambda_{T_e}$  being the gradient length ratio. In panel (b), the relations  $\lambda_{p_e} = 2/3 \lambda_{T_e}$  and  $\lambda_{p_e} = \lambda_{T_e}/2$  are depicted as a dashed and solid line, respectively.

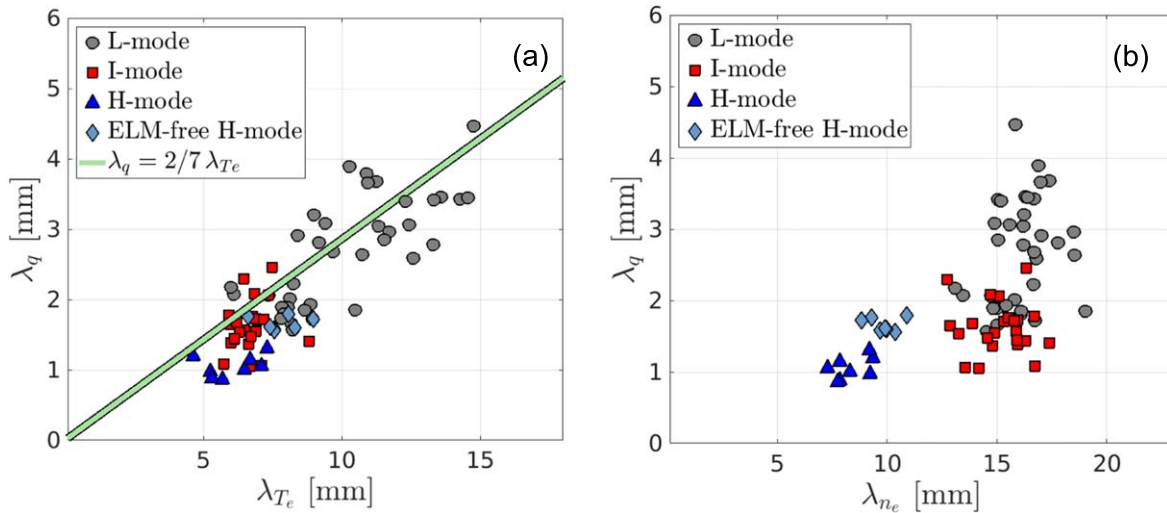


**Figure 8.** SOL power decay length  $\lambda_q$  against SOL electron temperature (a) and electron density (b) decay lengths. The light green line in panel (a) represents expected values of  $\lambda_q$  in the Spitzer–Härm electron heat conduction regime.

(i) *The nature of  $\lambda_q$  scaling with  $p_e^{95}$ .* The link between SOL and pedestal electron pressure gradients ultimately leads to a scaling of  $\lambda_q$  with  $p_e^{95}$ : if pedestal width and the separatrix pressure do not change significantly, a correlation is introduced between the electron pressure pedestal top and the pedestal gradients. At the same time, it has been shown that pedestal and SOL electron pressure gradients exhibit a linear correlation. Putting together these two findings, a correlation between  $p_e^{95}$  and  $\lambda_p^{\text{SOL}}$  appears. Considering now that  $\lambda_q$  and  $\lambda_p^{\text{SOL}}$  are related to each other (see figure 5(a)), the correlation between  $\lambda_q$  and  $p_e^{95}$  follows. This may be the explanation behind the Alcator C-Mod scaling as well and it could be supported by their observation of a correlation between  $\lambda_q$ ,  $\lambda_{p_e}$  and the pedestal pressure evolution [19].

(ii) *The connection between SOL and edge confined region.* At first glance, it may sound surprising that a SOL quantity ( $\lambda_{p_e}^{\text{SOL}}$ ), which is set by the competition between parallel and perpendicular transport, and  $L_{p_e}^{\text{ped}}$ , a quantity of the plasma confined region that is set by perpendicular transport, could be related; however, experimental profiles measured around the separatrix show one characteristic decay length when plotted in logarithmic scale [15, 18]. Also, simulations carried out with the 2D drift-fluid code ESEL [36] show no abrupt change of edge temperature and density profiles around the separatrix. These experimental and numerical evidences point towards a connection between near-SOL and pedestal regions. For completeness, it should be mentioned that in nitrogen seeded discharges at AUG, a de-correlation between pedestal

top electron pressure and SOL electron temperature decay length has been observed [38]; however, it could be that the aforementioned correlation between SOL and pedestal electron pressure gradients is still retained, with the difference being that in this case, a larger pedestal top value is achieved due to the inward shift of the pedestal profile (typical of N seeded discharges [39]). Evidence of a connection between SOL and confined edge region is also given by recent experiments carried out at the TJ-II stellarator [21]. It was observed that the turbulence spreading in the SOL (the nonlocal nonlinear growth rate of turbulence) decreases when a transport barrier in the plasma edge is present (i.e. when turbulence is reduced at the edge plasma). This suggests that the turbulence in the SOL comes from the confined edge region, tightly binding the turbulence in the SOL and confined edge region of fusion devices.

An interesting physical picture that allows us to interpret the observed correlation between SOL and pedestal pressure gradients is given in [18, 19]. As shown in these papers, the edge pressure gradient appears to be set by a critical-gradient (determined by electromagnetic fluid drift turbulence), rather than a classical diffusive-like transport. In other words, the edge electron pressure gradient adjusts to satisfy a marginal stability constraint. In such a picture, the correlation between near-SOL and pedestal gradients can be interpreted as the need for both gradients to satisfy the same marginal stability constraints.

In any case, the main consequence of these observations is that the pedestal electron pressure gradient and  $\lambda_q$  are linked. In other words, across the confinement regimes analyzed, it is difficult to combine a large  $\lambda_q$  with a steep pedestal electron pressure gradient. This would not be an obstacle to obtain high core pressures if the pedestal width could be freely enlarged and, consequently, high pedestal top values could be reached. Unfortunately, the pedestal width is not largely varying, except for some particular cases [39, 40]. Therefore, the highlighted coupling of SOL and pedestal electron pressure gradients may be an obstacle to finding a stable scenario that couples high core performances and a power exhaust solution. Turning our attention to ITER, the scaling law presented here predicts for the baseline  $I_p = 15$  MA and  $Q = 10$  inductive H-mode burning plasma scenario  $\lambda_{q,ITER} \simeq 0.6$  mm and it adds up to other experimental scaling laws [8, 11] that foreseen  $\lambda_{q,ITER}$  to be in the same range of values. Yet it should be mentioned that recent gyrokinetic [6] and fluid [7] simulations predict the ITER edge plasma to be in a turbulence dominated regime that is not achievable in present-day machines and that is expected to lead to larger  $\lambda_{q,ITER}$  values of about 5 mm. However, also in light of the correlation between pedestal and SOL electron pressure gradients found in this work, further investigations are needed to unveil whether such turbulence dominated regime will be compatible with the achievement of the desired high core plasma pressure.

## 8. Conclusions

A database that combines divertor  $\lambda_q$  measurements (from IR cameras) and SOL electron pressure, temperature and density decay lengths (from edge Thomson scattering) at the same time has been assembled at ASDEX Upgrade. The database encompasses different confinement regimes (L-mode, I-mode, inter-ELM H-mode and stationary ELM-free H-mode), different divertor geometries (open versus closed divertor) and different ion  $\nabla B$  drift directions (pointing to and away from the active X-point). Hence, this database allows us to study  $\lambda_q$  correlations that may hold for very different confinement regimes and divertor conditions. This approach may help unfold the physics that is ultimately setting  $\lambda_q$ , a key quantity that determines the operational window of ITER [2–4] and of any other next step fusion device. In analyzing the database, the following conclusions have been reached:

- (i) A cross-regime  $\lambda_q$  scaling is better described by a local edge parameter, i.e. the electron pressure at  $\rho_{pol} = 0.95$  ( $p_e^{95}$ ), than by global quantities, such as the volume-averaged plasma pressure  $\bar{p}$  or the average poloidal magnetic field  $\langle B_{pol} \rangle$ . The  $\lambda_q$  scaling found is:  $\lambda_q[\text{mm}] = 2.45 \pm 0.02 \times (p_e^{95}[\text{kPa}])^{-0.34 \pm 0.01}$ . It groups together all the confinement regimes analyzed, highlighting a possible unified physics mechanism setting  $\lambda_q$ .
- (ii) The power decay length  $\lambda_q$  is well correlated with both the SOL electron pressure decay length and the pedestal electron pressure gradient length. Hence, the edge electron pressure gradient, no matter if taken inside or outside the last closed flux surface, is found to be a robust local plasma parameter able to scale  $\lambda_q$  across all confinement regimes.
- (iii) SOL and pedestal electron pressure gradient are remarkably well correlated with each other across all confinement regimes. This observation may suggest that both near-SOL and pedestal electron pressure gradients are controlled by a critical-gradient transport paradigm, in which both near-SOL and pedestal edge electron pressure gradients adjust themselves to satisfy the same marginal stability constraint, as suggested in [18, 19]. The same observation may also point towards an important role of the turbulence spreading [20] (i.e. the non-local component of turbulence) in setting the radial transport in the SOL, as suggested in [21].
- (iv) The Spitzer–Härm electron heat conduction regime is a reasonable approximation to estimate  $\lambda_q$  in these attached plasmas, i.e.  $\lambda_q = 2/7 \lambda_{T_e}$ . Nonetheless, interestingly  $\lambda_q$  scaling laws better correlate with edge electron pressure parameters, rather than electron temperature ones, see table 2. We believe that this is due to the close correlation between pedestal and SOL electron pressure gradients, which allows one to better characterize a SOL quantity such as  $\lambda_q$  with the plasma parameters of the confined region.

The main implication of this work is that  $\lambda_q$  scales unfavourably with  $p_e^{95}$  and/or with the edge electron pressure

gradient. In particular, an increase of core plasma pressure (which means a rise of  $p_e^{95}$  or a steepening of the edge electron pressure gradient) is statistically associated with a reduction of  $\lambda_q$ . In other words, across the confinement regimes analyzed, it is difficult to combine a large  $\lambda_q$  with a steep pedestal electron pressure gradient. This may be an obstacle to finding a stable scenario that couples high core performances and a power exhaust solution, which must, in any case, rely on detachment.

## Acknowledgments

The authors are grateful for discussions with P Manz, M Hosner and D Brida. This work has been carried out within the framework of the EUROfusion Consortium and has received funding from the Euratom research and training programme 2014–2018 and 2019–2020 under grant agreement No 633 053. The views and opinions expressed herein do not necessarily reflect those of the European Commission.

## ORCID iDs

D Silvagni  <https://orcid.org/0000-0003-2103-3592>  
 T Eich  <https://orcid.org/0000-0003-3065-8420>  
 M Faitsch  <https://orcid.org/0000-0002-9809-7490>  
 T Happel  <https://orcid.org/0000-0003-4364-9363>  
 D Nille  <https://orcid.org/0000-0002-4541-320X>  
 L Gil  <https://orcid.org/0000-0002-9970-2154>

## References

- [1] Pitts R *et al* 2013 *Proc. 20th Int. Conf. on Plasma-Surface Interactions in Controlled Fusion Devices; J. Nucl. Mater.* **438** S48–56
- [2] Kukushkin A *et al* 2013 *Proc. 20th Int. Conf. on Plasma-Surface Interactions in Controlled Fusion Devices; J. Nucl. Mater.* **438** S203–7
- [3] Reinke M L *et al* 2017 *Nucl. Fusion* **57** 034004
- [4] Goldston R J *et al* 2017 *Plasma Phys. Control. Fusion* **59** 055015
- [5] Goldston R 2011 *Nucl. Fusion* **52** 013009
- [6] Chang C S *et al* 2017 *Nucl. Fusion* **57** 116023
- [7] Xu X *et al* 2019 *Nucl. Fusion* **59** 126039
- [8] Eich T *et al* 2013 *Nucl. Fusion* **53** 093031
- [9] Zohm H 1996 *Plasma Phys. Control. Fusion* **38** 105–28
- [10] Leonard A W 2014 *Phys. Plasmas* **21** 090501
- [11] Brunner D, LaBombard B, Kuang A and Terry J 2018 *Nucl. Fusion* **58** 094002
- [12] Gil L *et al* 2019 *46th European Physical Society Conf. on Plasma Physics* (<http://ocs.ciemat.es/EPS2019PAP/pdf/O2.110.pdf>)
- [13] Sieglin B, Faitsch M, Herrmann A, Brucker B, Eich T, Kammerloher L and Martinov S 2015 *Rev. Sci. Instrum.* **86** 113502
- [14] Kurzan B and Murmann H D 2011 *Rev. Sci. Instrum.* **82** 103501
- [15] Sun H J, Wolfrum E, Eich T, Kurzan B, Potzel S and Stroth U 2015 *Plasma Phys. Control. Fusion* **57** 125011
- [16] Faitsch M, Sieglin B, Eich T, Sun H J and Herrmann A 2015 *Plasma Phys. Control. Fusion* **57** 075005
- [17] Happel T *et al* 2019 *Nucl. Mater. Energy* **18** 159–65
- [18] LaBombard B, Hughes J, Mossessian D, Greenwald M, Lipschultz B, Terry J and the Alcator C-Mod Team 2005 *Nucl. Fusion* **45** 1658–75
- [19] LaBombard B *et al* 2011 *Phys. Plasmas* **18** 056104
- [20] Manz P, Ribeiro T T, Scott B D, Birkenmeier G, Carralero D, Fuchert G, Müller S H, Müller H W, Stroth U and Wolfrum E 2015 *Phys. Plasmas* **22** 022308
- [21] Grenfell G, van Milligen B, Losada U, Ting W, Liu B, Silva C, Spolaore M and Hidalgo C 2018 *Nucl. Fusion* **59** 016018
- [22] Meyer H *et al* 2019 *Nucl. Fusion* **59** 112014
- [23] Ryter F, Suttrop W, Brüsehaber B, Kaufmann M, Mertens V, Murmann H, Peeters A G, Stober J, Schweinzer J, Zohm H and Team A U 1998 *Plasma Phys. Control. Fusion* **40** 725–9
- [24] Whyte D *et al* 2010 *Nucl. Fusion* **50** 105005
- [25] Sieglin B, Eich T, Faitsch M, Herrmann A and Scarabosio A 2016 *Plasma Phys. Control. Fusion* **58** 055015
- [26] ITER Physics Expert Group on Confinement and Transport/ITER Physics Expert Group on Confinement Modelling and Database and ITER Physics Basis Editors 1999 *Nucl. Fusion* **39** 2175–249
- [27] Mlynek A, Schramm G, Eixenberger H, Sips G, McCormick K, Zilker M, Behler K, Eheberg J and ASDEX Upgrade Team 2010 *Rev. Sci. Instrum.* **81** 033507
- [28] Nille D, von Toussaint U, Sieglin B and Faitsch M 2018 *Bayesian Inference and Maximum Entropy Methods in Science and Engineering* (Cham: Springer) (<https://doi.org/10.1007/978-3-319-91143-4>)
- [29] Herrmann A, Junker W, Gunther K, Bosch S, Kaufmann M, Neuhauser J, Pautasso G, Richter T and Schneider R 1995 *Plasma Phys. Control. Fusion* **37** 17–29
- [30] Eich T, Sieglin B, Scarabosio A, Fundamenski W, Goldston R J, Herrmann A and (ASDEX Upgrade Team) 2011 *Phys. Rev. Lett.* **107** 215001
- [31] Stangeby P 2000 *The Plasma Boundary of Magnetic Fusion Devices* (Bristol: Institute of Physics Publishing)
- [32] Fischer R, Fuchs C J, Kurzan B, Suttrop W and Wolfrum E 2010 *Fusion Sci. Technol.* **58** 675–84
- [33] Nielsen A *et al* 2019 *Nucl. Fusion* **59** 086059
- [34] Faitsch M *et al* 2018 *Plasma Phys. Control. Fusion* **60** 045010
- [35] Schneider P A *et al* 2012 *Plasma Phys. Control. Fusion* **54** 105009
- [36] Militello F, Fundamenski W, Naulin V and Nielsen A H 2012 *Plasma Phys. Control. Fusion* **54** 095011
- [37] Eich T *et al* 2019 *46th European Physical Society Conference on Plasma Physics* (<http://ocs.ciemat.es/EPS2019PAP/pdf/O4.106.pdf>)
- [38] Sun H, Wolfrum E, Eich T, Kurzan B, Kallenbach A, Happel T and Stroth U 2019 *Plasma Phys. Control. Fusion* **61** 014005
- [39] Dunne M G *et al* 2016 *Plasma Phys. Control. Fusion* **59** 014017
- [40] Chen X *et al* 2016 *Nucl. Fusion* **57** 022007